

RSC Advances



This is an *Accepted Manuscript*, which has been through the Royal Society of Chemistry peer review process and has been accepted for publication.

Accepted Manuscripts are published online shortly after acceptance, before technical editing, formatting and proof reading. Using this free service, authors can make their results available to the community, in citable form, before we publish the edited article. This *Accepted Manuscript* will be replaced by the edited, formatted and paginated article as soon as this is available.

You can find more information about *Accepted Manuscripts* in the [Information for Authors](#).

Please note that technical editing may introduce minor changes to the text and/or graphics, which may alter content. The journal's standard [Terms & Conditions](#) and the [Ethical guidelines](#) still apply. In no event shall the Royal Society of Chemistry be held responsible for any errors or omissions in this *Accepted Manuscript* or any consequences arising from the use of any information it contains.

Fabrication and photoelectrochemical properties of $\text{TiO}_2/\text{CuInS}_2/\text{Bi}_2\text{S}_3$ core/shell/shell nanorods electrodes

Yanling Wan^{a,b}, Minmin Han^{a,b}, Limin Yu^{a,b}, Junhong Jia^{a,*} and Gewen Yi^{a,*}

^aState Key Laboratory of Solid Lubrication, Lanzhou institute of Chemical Physics, Chinese Academy of Sciences,

Lanzhou, 730000, PR China.

^bUniversity of Chinese Academy of Sciences, Beijing 10049, PR China.

* Corresponding author, Fax: +86 931 4968611
E-mail address: jhjia@licp.cas.cn (J. Jia), gwyi@licp.cas.cn (G. Yi)

ABSTRACT

TiO₂/CuInS₂/Bi₂S₃ core/shell/shell (CSS) nanorods (NRs) electrodes were synthesized by successive ionic layer adsorption and reaction (SILAR) method and their use were assigned to the photoelectrodes for high performance in a photoelectrochemical (PEC) cell, where the non-toxic materials narrow bandgap CuInS₂ and Bi₂S₃ were selected to expand the light absorption range to the near-infrared region. The uniform Bi₂S₃ layer was directly covered on the prior coated CuInS₂ layer on TiO₂ NRs to prevent the polysulfide electrolytes corrosion of CuInS₂. The morphology, crystal structure, optical properties and PEC performance of plain TiO₂, single TiO₂/CuInS₂ core/shell (CS) and TiO₂/CuInS₂/Bi₂S₃ CSS NRs were investigated in detail. The deposition cycles of the CuInS₂ and Bi₂S₃ on TiO₂ NRs were optimized to enhance the PEC performance of TiO₂/CuInS₂/Bi₂S₃ CSS composites electrodes. The results show that TiO₂/CuInS₂/Bi₂S₃ CSS obtained enhanced photoconversion efficiency (6 times higher than that of plain TiO₂ and 1.5 times than TiO₂/CuInS₂ CS). Therefore, the construction of CSS nanostructured composites electrodes through coupling single core/shell nanostructures with another narrow gap semiconductor shell suggests a promising design for improving the absorption efficiency and PEC performance of photoelectrodes.

1. Introduction

One dimensional orderly Single-crystalline TiO₂ nanorod TiO₂ nanostructures including nanorods (NRs), nanotubes (NTs) and nanowires (NWs) are important n-type semiconductor materials, which have drawn considerable attention in

photocatalysis and solar cells because of their unique optical and electronic characteristics, which accordingly lead to accept and transport electron to the counter electrodes materials¹⁻³. And compared with the conventional TiO₂ nanoparticle thin films, Single-crystalline TiO₂ nanorod arrays provide a direct channel for carrier transmission and can efficiently ensure the separation and collection of photo-excited electrons⁴. However, TiO₂ is a wide-band gap semiconductor ($E_g \approx 3.2\text{eV}$), only can absorb the short of ultraviolet in the solar spectrum, resulting in its high recombination rate of photogenerated electron and hole⁵. Researchers have adopted many methods to expand TiO₂ spectral range, and improve the energy conversion efficiency, such as dye-sensitized solar cell (DSSC)^{6,7} and semiconductor sensitized solar cell (SSSC)^{8,9}. Due to the disadvantages of high cost and unstable performances for DSSC, much attention has been transferred to the inorganic narrow band-gap semiconductor sensitized solar cells, because the sensitizers enables produce highly efficient multiple charge carriers and their optical properties can be tailored by simply changing their size¹⁰.

Various narrow band-gap materials including CdS^{11,12}, CdSe¹³, PbS¹⁴, Bi₂S₃^{15,16} and CuInS₂¹⁷ have been synthesized as sensitizers deposited on the wide-bandgap semiconductor by controlling the particle size to improve the absorption. Among these sensitizers, toxicity is a problem worth considering. Comparing with CdS and PbS, Bi₂S₃ (BS) and CuInS₂ (CIS) are almost non-toxic materials and both have a high absorption coefficient of α ($\sim 10^5\text{ cm}^{-1}$), direct band gap energy (1.3eV and 1.51eV respectively)¹⁸⁻²⁰, which can promote the absorption extending to the visible region

and even to the near-infrared light area, exhibit improved performance in light harvesting. In addition, comparing with TiO_2 , both Bi_2S_3 and CuInS_2 have higher conduction band edge^{21, 22}, which can increase the possibility to electron injection from conduction band of sensitizers to the one dimensional TiO_2 . The new nanostructure of two kinds of different band energy co-sensitization to form core/shell/shell (CSS) have emerged to construct light energy harvesting assemblies²³. The CSS nanostructure can not only achieve extraordinary performance because the outer shell serves as a potential barrier which confines the charge carriers in the region, but also can suppress the recombination of photo-excited electron-hole pairs and protect core material from chemical erosion^{24, 25}. To date, the studies of CSS NRs structure are rare, but ~~studies of it~~ that would attract more attention because of its excellent PEC performance of CSS NRs structure. Recently, Ai et al. reported a Bi_2S_3 -coated TiO_2 core/shell structure by SILAR method²⁶. The hetero-structured $\text{TiO}_2/\text{Bi}_2\text{S}_3$ exhibited an enhanced photocurrent density ~~higher than~~ compared with that of pristine TiO_2 . Song et al. deposited a uniform PbS nanoparticle on ZnO nanorods turning into core/shell structure and the power conversion efficiency of ZnO/PbS CEs increased tremendously compared to that with planar Pt and bare PbS CE²⁷. Guo et al. synthesized TiO_2/CIS core/shell nanoarrays via a simple SILAR technique and polyol reduction routes²⁸. Wang et al. reported a hierarchical double-shell $\text{TiO}_2/\text{ZnSe}/\text{CdSe}$ nanocable arrays and obtained the power conversion efficiency up to 1.33% through optimization the thickness of ZnSe layer³. Han et al. synthesized the $\text{ZnO}/\text{ZnS}/\text{MxS}$ CSS nanorods by a versatile chemical conversion

method based on the ion-by-ion growth mechanism and the hydrogen generation efficiency is up to 15.92%²⁹.

In general, two major methods ex-situ and in-situ have been applied to deposit metal sulfide quantum dots on substrates^{30,31}. The ex-situ method has been reported with low power conversion efficiency due to the long carbon chain organic ligands existence and low coverage of quantum dots on the electrode surface. The in-situ synthesis techniques such as chemical bath deposition (CBD) and successive ionic layer adsorption and reaction (SILAR) are the most widely used methods, which can result in a high surface coverage of QDs on the electrode surfaces³². In present work, we fabricated the TiO₂/CuInS₂/Bi₂S₃ CSS nanorods by SILAR method. The Bi₂S₃ layer was directly covered on the prior coated CuInS₂ layer on TiO₂ NRs to prevent the polysulfide electrolytes corrosion of CuInS₂. The deposition cycles of the CuInS₂ and Bi₂S₃ on TiO₂ NRs were optimized to enhance the PEC performance of TiO₂/CuInS₂/Bi₂S₃ CSS electrodes. The optical properties and PEC performances of TiO₂/CIS single layer core/shell (CS) nanorods was also investigated for comparing with the double layer CSS structure electrode. It is expected to exploit the CSS structure for the potential application of sensitized solar cell.

2. Experimental details

2.1 Preparation of TiO₂ nanorods

The TiO₂ NR arrays were directly grown on transparent FTO glass using the hydrothermal synthesis method similar to Li's report³³. In the typical synthesis

process, the FTO substrates were ultrasonically cleaned for 30min in a mixed solution of deionized water, acetone, 2-propanol with volume ratios of 1:1:1 and finally dried under N_2 flow. 15mL of deionized water was mixed with 15 mL of concentrated hydrochloric acid (36.5%-38% by weight) under magnetic stirring for 5 min, 0.2 mL titanium tetrachloride was added and the solution was keep stirring another 5 min. After that, the FTO substrates were placed at a stainless steel autoclave in 50 mL with the conducting side facing down. The precursor solution was added and the reaction was kept at 180 °C for 2 h. Then, the autoclave was cooled to room temperature under flowing water, and the FTO substrates were rinsed with deionized water for several times then dried in ambient air.

2.2 Fabrication of TiO_2 /CIS core/shell nanorods

The TiO_2 /CIS core-shell NR arrays were prepared via a successive ionic layer adsorption and reaction (SILAR) method similar to the literature³⁴. Briefly, the TiO_2 NR electrodes were successively immersed in three different precursor solutions contained $InCl_3 \cdot 4H_2O$ (5 mM), $CuCl_2 \cdot 2H_2O$ (5 mM) and $Na_2S \cdot 9H_2O$ (50 mM) for about 20 s each, respectively. After each dipping in precursor solution, the samples were rinsed in deionized water to remove the extra ions which were not adsorbed. After several cycles, the deposited samples were annealed in the tube furnace at 370 °C for 30 min under nitrogen protection and were labeled as TiO_2 /CIS(x) core/shell NR, where x refer to the number of CIS SILAR cycles.

2.3 Fabrication of TiO_2 /CIS/BS CSS nanorods

A four beaker system is used for Bi_2S_3 nanoparticles coating refer to the literature⁵. To begin with, the TiO_2/CIS core/shell nanostructure electrode was immersed in the 2 mM precursor acetone solution of $\text{Bi}(\text{NO}_3)_3 \cdot 5\text{H}_2\text{O}$ for 60 s. Then, the electrode was rinsed in acetone for 30 s to remove the loosely bounded ions. Thirdly, the electrode sample was soaked in the anionic precursor which contains 0.13 M $\text{Na}_2\text{S} \cdot 9\text{H}_2\text{O}$ aqueous solution for 60 s for the adsorption of sulfur ions to react with bismuth ions. After immersing, the sample was rinsed in deionized water for 30 s. Finally, the samples were treated in a vacuum drying oven at 60 °C 12 h and were labeled as $\text{TiO}_2/\text{CIS}(x)/\text{BS}(y)$, where y refers to the number of Bi_2S_3 SILAR cycles.

2.4 Characterization

The morphology of the sample was observed by a scanning electron microscope (FESEM, JSM-6701F, and Japan), a transmission electron microscope (TEM, TF20) and high resolution transmission microscope (HRTEM). The crystal structure of the sample was detected by a X-ray diffractometer (XRD, Rigaku D/max-2400, Japan) using Cu K α radiation ($\lambda=0.15418$ nm) in the 2θ range of 20°–80° and at a scanning speed of 10°min⁻¹. The chemical composition of the sample was identified by X-ray photoelectron spectroscopy (XPS, PHI-5702). The optical properties were carried out by a LabTech (China) spectrophotometer within the wavelength range of 200-1000 nm.

2.5 Photoelectrochemical measurements

The PEC measurements were performed by a standard three-electrode system,

which was composed of electrolytic cell carrying a quartz window linked with the electrochemical workstation (CH instruments, model CHI660d). The TiO₂/CIS/BS CSS nanorods electrodes were used as the working electrode, platinum mesh as the counter electrode and saturated calomel electrode (SCE) as the reference electrode. The electrolyte were 0.05 M Na₂S·9H₂O and 0.95 M Na₂SO₃ aqueous solution. The illumination source was a xenon lamp, which can produce an intensity of 100 mW cm⁻² in the sample surface, and the photocurrent of the working electrode was carried out by a bias of from -1.0 V to 0.9 V.

3. Results and discussion

3.1 Morphology and structure characterization

Fig. 1a and b show the top-view and cross-sectional FESEM images of bare TiO₂ nanorods arrays. It can be seen that the TiO₂ NRs vertically grow on the FTO substrate and appear smooth surface. The individual NR is tetragonal in shape with square top facets which is consistent with Liu's work¹. The average length of NRs is approximately 1.9 μm and about 110 nm in diameter. Fig. 1c and d display that the surfaces of TiO₂ nanorods become rough after 5 cycles CIS deposition. The nanoparticles are uniformly arranged on the surface of TiO₂ NRs without aggregation. When TiO₂/CIS(5) electrode immersed in precursor solutions of Bi³⁺ and S²⁻, the number of nanoparticles increases significantly (Fig. 1e and f), which implies that the BS nanocrystals deposited on the surface of CIS layer and to be a core/shell structure based on the core of TiO₂/CIS. Therefore, a double sheath TiO₂/CSS/BS CSS NRs

arrays were deposited on FTO substrate.

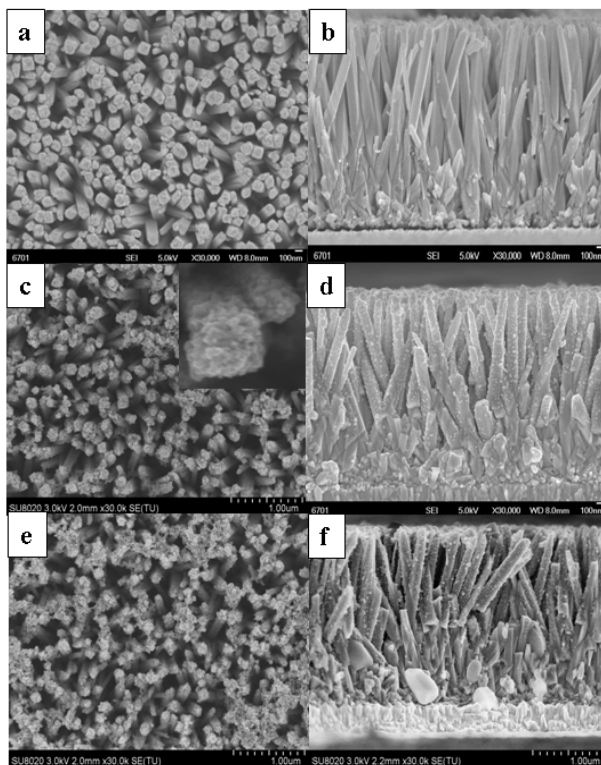


Fig.1 Top-view and cross-sectional FESEM images of the bare TiO₂ nanorods array, (a), (b), TiO₂/CIS (5) core/shell structure (c), (d) and TiO₂/CIS (5)/BS (1) CSS structure (e), (f)

Fig. 2a and 2b show a typical TEM and HRTEM images of TiO₂/CIS(5) core/shell NRs. It can be seen that the CIS nanoparticles with a size ranging from 5 nm to 8 nm were uniformly covered on the TiO₂ nanorods, and the nanoparticles were connected each other form into a layered thin film. Distinguishable lattice fringes in the HRTEM image (Fig.2b) verified the high crystallinity of the CIS nanoparticles. The distance between lattice fringes is of 0.327 nm and 0.305 nm, corresponding to the (112) and (103) planes of chalcopyrite phase CIS [JCPDS file no.85-1575], respectively. The thickness of the CIS shell increased with the increasing of SILAR

cycles and the TiO_2 NR is decorated by a layer of 10-12 nm film when SILAR cycles of CuInS_2 is up to 7 times (Fig. 2c). Fig. 2d and 2e show TEM and HRTEM images of $\text{TiO}_2/\text{CIS}(5)/\text{BS}(1)$ CSS NRs, respectively. The surfaces of the NRs become rougher than that of $\text{TiO}_2/\text{CIS}(5)$ in Fig. 2a, and the Bi_2S_3 particles with a size of 5-8 nm continuously arranged outside of CIS layer. The lattice distances correspond well with the (221) plane of bismuthinite Bi_2S_3 [JCPDS file no.06-0333] and (112) plane of chalcopyrite phase CuInS_2 [JCPDS file no.85-1575] (Fig. 2e). The elemental distribution maps (Fig. 2f) taken across the NR in white square in Fig. 2d illuminates that the Cu, In, S and Bi elements distribute almost uniformly over the whole TiO_2 NR. Consequently, the $\text{TiO}_2/\text{CIS}/\text{BS}$ CSS NR arrays can be successfully prepared by SILAR method.

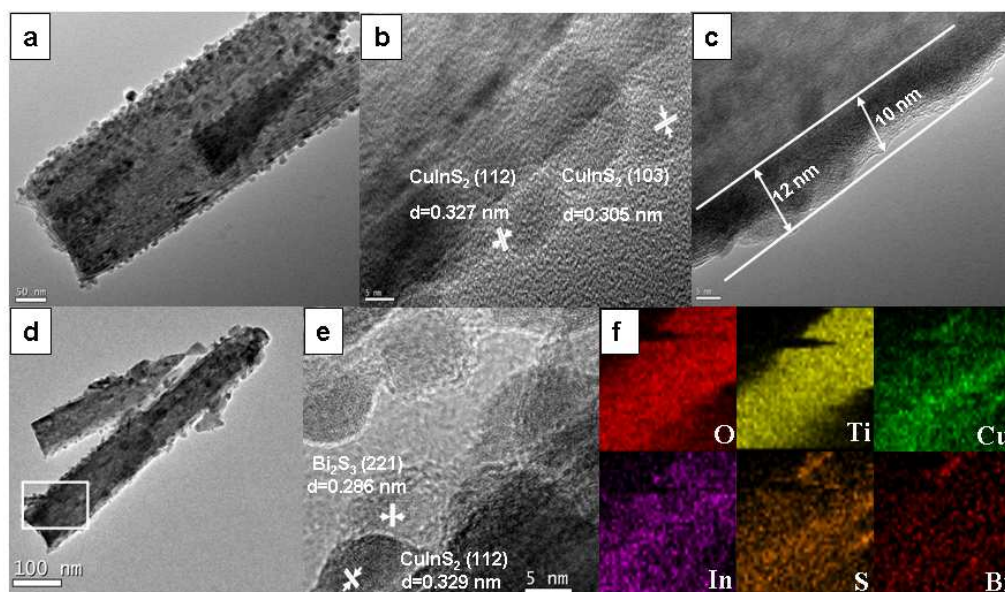


Fig. 2 TEM image and HRTEM image of $\text{TiO}_2/\text{CIS}(5)$ core/shell structure (a), (b), and $\text{TiO}_2/\text{CIS}(5)/\text{BS}(1)$ core/shell structure (c), $\text{TiO}_2/\text{CIS}(5)/\text{BS}(1)$ CSS structure electrode (d), (e), corresponding STEM-EDX elemental mapping (f) for white square in Fig. 2d.

Fig. 3 shows the XRD patterns of the TiO₂ NRs, TiO₂/CIS core/shell NRs and TiO₂/CIS/BS CSS NRs, respectively. For TiO₂, except the FTO substrate, all the diffraction peaks are consistent with the standard tetragonal rutile phase TiO₂ (SG, P42/mnm, JCPDS No. 75-1748, a = b = 0.4594 nm and c = 0.2959 nm) (curve a). In curve b, the diffraction peaks located at the diffraction angle of 27.8°, 46.3°, 55°, are corresponding to the crystal planes (112), (220)/(204) and (312)/(116) of the chalcopyrite phase (JCPDS No. 85-1575, a = b = 0.5523 nm and c = 1.1133nm). The relatively weak diffraction peaks may own to the thin layer of CIS on TiO₂ NRs. Meanwhile, the diffraction peaks at 25.2° and 28.6° can be indexed to the crystal planes of (111) and (230) planes of bismuthinite Bi₂S₃ (JCPDS No.06-0333, a=1.115nm, b=1.13nm, c=0.3981nm) without other impurities (curve c). The XRD results suggest that the CuInS₂ and Bi₂S₃ nanocrystals have been successfully coated on the surfaces of the TiO₂ NRs.

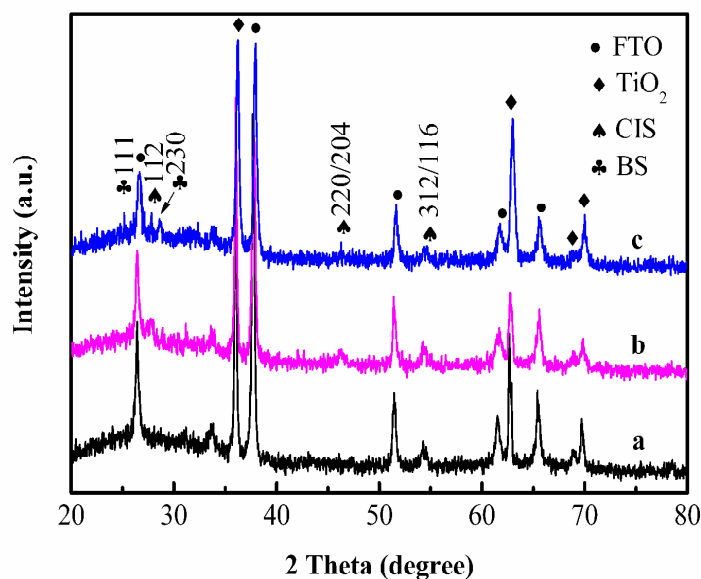


Fig. 3 XRD patterns of TiO₂ (a), TiO₂/CIS (b) and TiO₂/CIS/BS nanorods (c).

In order to further investigate the valence states of elements and composition in the TiO₂/CIS/BS CSS nanorods, the XPS analysis was conducted as shown in Fig. 4. It can be found that the main components of sample are Ti, O, Cu, In, S, Bi elements. The elements binding energy of high resolution spectrum was revised refer to the binding energy of C1s (284.8 eV). Fig. 4a shows the high-resolution spectrum of Ti2p, the peaks of binding energies at 458.8 eV and 464.8 eV were assigned to Ti2p_{3/2} and Ti2p_{1/2}. These two peaks are separated by 6.0 eV, which indicates Ti⁴⁺ existing in rutile phase TiO₂³⁵. The binding energies of O1s at 529.9 eV and 531.8 eV that were attributed to the crystal lattice oxygen (Ti-O) and different kinds of physical absorbed oxygen (H-O) in the film (Fig. 4b)³⁶. Moreover, the strong and sharp peaks of Ti and O reveal that it exists as chemistry states. The Cu2p core split into 2p_{3/2} (932.1 eV) and 2p_{1/2} (952.1 eV), can be assigned to Cu(I) according to the literature¹⁹ (Fig. 4c). In addition, the binding energy of Cu2p indicates that the CIS was deposited successfully on TiO₂ NRs without Cu(II) (942 eV). The binding energies of In3d are 444.8 eV (In3d_{5/2}) and 452.4 eV (In3d_{3/2}), suggesting that In³⁺ was existed in CIS nanocrystals (Fig. 4d)³⁷. The S core binding energy displayed in Fig. 4e contains two peaks, the peaks of binding energy at 161.9eV and 163.2eV are assigned to Cu-S bond and In-S bond structure in CIS, that are not a symmetric peak owing to the responses of Cu-S and In-S, which consistent with that CuInS₂³⁸. The Bi4f peaks of the sample is located in 158.5 eV (Bi4f_{7/2}) and 163.8eV (Bi4f_{5/2}), which are in agree with that of Bi₂S₃ in literature³⁹. Combined with the XRD analysis, it can be corroborated that the CIS and BS nanoparticles are deposited on the surface of TiO₂ nanorods successfully

and there is no obviously impurities exist in the as-obtained $\text{TiO}_2/\text{CIS}/\text{BS}$ CSS nanorods.

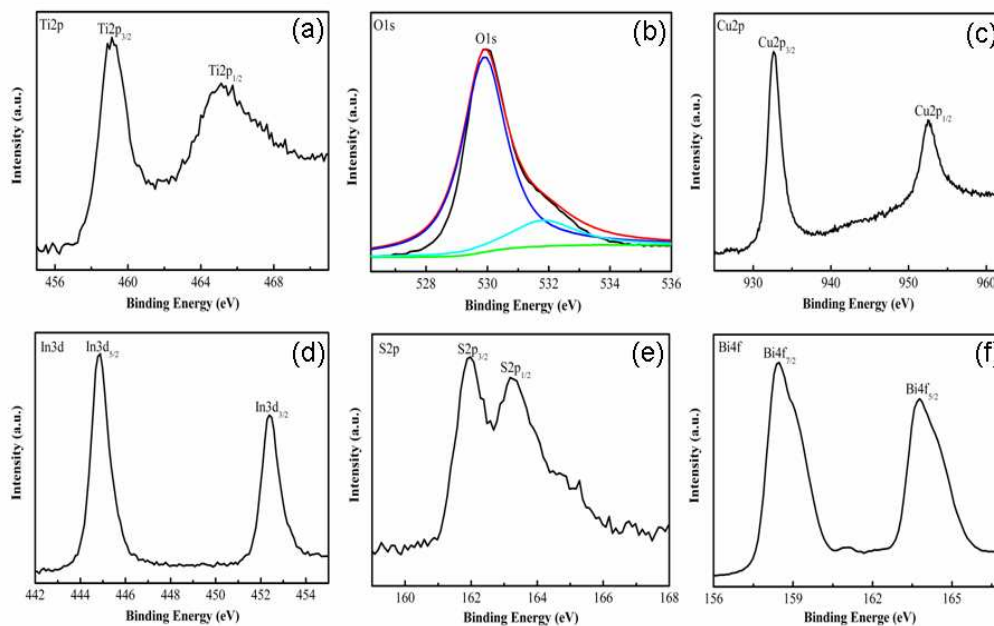


Fig. 4 High-resolution XPS spectra of O 1s (a), Ti 2p (b), Cu 2p (c), In 3d (d), S 2p (e), Bi 4f (f) for $\text{TiO}_2/\text{CIS}/\text{BS}$ CSS NRs.

3.2 Optical and photoelectrochemical properties of $\text{TiO}_2/\text{CIS}/\text{BS}$ CSS NRs

Fig. 5a gives the Uv-vis absorption spectra of TiO_2 NRs and TiO_2/CIS core/shell NRs with different SILAR cycles of CIS. An increased optical absorption is observed for the TiO_2/CIS films compared with that of the plain TiO_2 nanorods. The absorption edge of plain TiO_2 is only 410 nm, while that enlarge to 600-800 nm after CuInS_2 deposition, which confirms that the CuInS_2 can effectively improve the light absorption of the TiO_2 nanorods. Moreover, the light absorption intensity was gradually improved with the increase of SILAR cycles of CIS and caused a red shift. The photocurrent response of TiO_2 NRs and TiO_2/CIS NRs under a 0.2 V bias vs. SCE

reference electrode was shown in Fig. 5b. It can be seen that the plain TiO₂ NRs and TiO₂/CIS NRs exhibited a stable light current and low dark current under the 100 mW cm⁻² simulated sunlight. Which indicate that the electrode of plain TiO₂ and TiO₂/CIS have fewer defects and exhibit excellent crystallinity. Moreover, the photocurrent densities of TiO₂/CIS electrodes present the tendency of firstly increase then decrease with the increasing of CIS SILAR cycles. The maximum current density about 0.32 mA cm⁻² of TiO₂/CIS was obtained at the 5 SILAR cycles of CIS. Compare with plain TiO₂ NR (0.05 mA cm⁻²), the obvious improvement of photocurrent density for TiO₂/CIS NRs illustrates that the excited electrons of CIS can smoothly inject into the TiO₂ conduction band through one-dimensional TiO₂ channel.

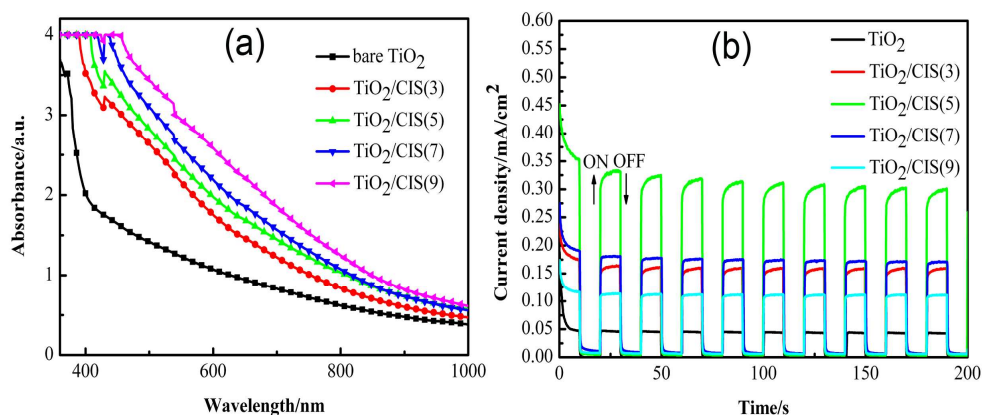


Fig. 5 Uv-vis absorption spectra of TiO₂ NRs and TiO₂/CIS core/shell NRs with different cycles

(a), photocurrent responses of TiO₂ NRs and TiO₂/CIS core/shell NRs with different cycles (b).

Fig. 6 reveals the UV-vis absorption spectra and photocurrent responses of TiO₂/CIS(5)/BS CSS NRs. It is noteworthy that the optical absorption of CSS NRs extends to near-infrared light region and the absorption edges enlarge to 800-900 nm with the increasing of BS SILAR circles (Fig.6a). Moreover, the light absorption

intensities of TiO₂/CIS(5)/BS CSS continuously increased with the increasing of BS SILAR cycles when compare to the TiO₂/CIS single shell. Fig. 6b displays the photocurrent responses of TiO₂/CIS(5)/BS CSS NRs with different SILAR cycles of BS. It was found that the photocurrent densities decreased with the increasing of Bi₂S₃ SILAR cycles and the TiO₂/CIS(5)/BS(1) CSS NRs holds the highest photocurrent density about 0.42 mA cm⁻². The possible reason is that the increased SILAR cycles of Bi₂S₃ results in the thicker outer shell, that will increase the internal recombination ratio of the charge carriers and the thicker outer shell will also restrain the electrolyte to penetrate in²⁴. It can also be deduced that the CSS structures are able to show improved photoelectronic performance through adjust that the shell thickness.

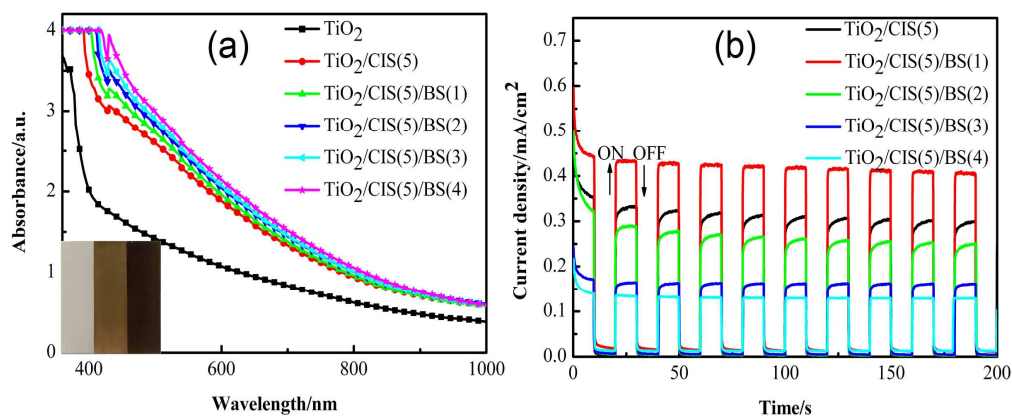


Fig. 6 Uv-vis absorption spectra of TiO₂/CIS(5)/BS CSS NRs (a), and photocurrent responses of TiO₂/CIS(5)/BS CSS NRs (b) under a 0.2 V bias vs. SCE reference electrode with an illumination of 100mW cm⁻² in 0.05 M Na₂S and 0.95 M Na₂SO₃ aqueous solution.

Fig. 7 presents the electrochemical impedance spectrum (EIS) Nyquist plots of TiO₂ NRs, TiO₂/CIS(5) NRs and TiO₂/CIS(5)/BS(1) NRs electrodes which measured in 0.05 M Na₂S and 0.95 M Na₂SO₃ aqueous solution in dark and under visible light

irradiation. Only one circular arc appears in the Nyquist plots and it reflects the interface impedance between electrode and electrolyte⁴⁰. The results suggest that the EIS of TiO₂ NRs electrodes in dark and under visible light are almost two straight lines because the plain TiO₂ almost has no response to the visible light. However, the composite electrodes of TiO₂/CIS(5) shows smaller resistance-circles than plain TiO₂ whether in dark or visible light. This can be attributed to the efficient separation of photo-generated electron-hole pair and high rate of electron injection between the interfaces of heterojunction and electrolyte for the composite electrodes⁴¹. After the deposition of BS, the resistance-circle of TiO₂/CIS(5)/BS(1) is higher than that of TiO₂/CIS(5), which is due to the larger resistance of Bi₂S₃ itself than CuInS₂. The charge transfer resistance in the interface gradually reduce in the following order: TiO₂, TiO₂/CIS(5)/BS(1), TiO₂/CIS(5), implying a greater conductivity of TiO₂/CIS(5) electrode and a faster charge transfer rate in its surface. Meanwhile, it can be seen that the resistance for each electrode under visible light is less than that in dark, which indicates that the light enable to reduce the charge transfer resistance in the interface of electrode/electrolyte.

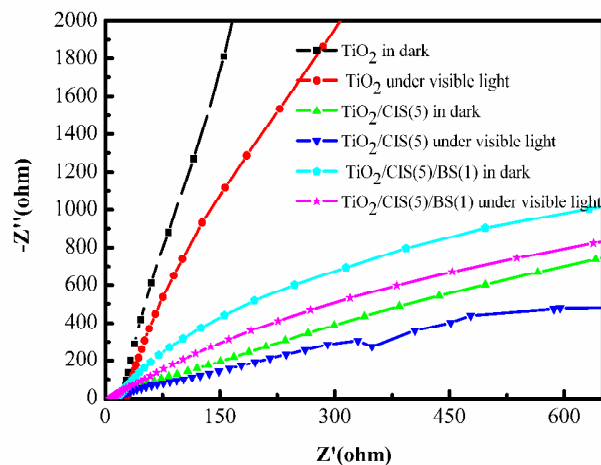


Fig. 7 The electrochemical impedance spectrum (EIS) Nyquist plots of TiO₂, TiO₂/CIS (5) and TiO₂/CIS (5)/BS (1) electrodes in dark and under visible light.

Fig. 8a shows the photocurrent density versus potential curves with TiO₂, TiO₂/CIS(5) CS and TiO₂/CIS(5)/BS(1) CSS NRs electrodes in dark and under the visible-light illumination of 100 mW cm⁻², respectively. The dark currents of three electrodes are almost close to zero. While under the visible light, the photocurrent density of each electrode is enhanced with the bias moving to positive direction. The TiO₂/CIS/BS electrode obtains the highest saturated photocurrent density (0.62 mA cm⁻²) than that of the other electrodes under the bias potential range from -1.0 to 0.9V. Fig. 8b shows the corresponding photoconversion efficiency (η) of three electrodes according to following equation⁴²:

$$\begin{aligned}\eta (\%) &= [(\text{total power output} - \text{electrical power input}) / \text{light power input}] \times 100 \\ &= j_p [E_{\text{rev}}^0 - | E_{\text{app}} |] \times 100 / (I_0)\end{aligned}$$

where j_p is the photocurrent density (mA cm⁻²), E_{rev}^0 is the standard state-reversible potential, which is 1.23 V (vs. NHE), and the applied potential is $E_{\text{app}} = E_{\text{meas}} - E_{\text{aoc}}$, where E_{meas} is the electrode potential (vs. SCE) of the working electrode, E_{aoc} is the open circuit electrode potential (vs. SCE) of the same working electrode under the same illumination and in the same electrolyte. It can be concluded that construction of CSS structure is an effective way to enhance the photoconversion efficiency for that the maximum photoconversion efficiency of TiO₂/CIS/BS CSS electrode is 0.44%, while that of the plain TiO₂ NRs electrode and TiO₂/CIS CS electrode are 0.07%, 0.28%, respectively. Apparently, the photoelectric performance

of the TiO₂/CIS/BS electrodes has been enhanced significantly by the Bi₂S₃ layer, this phenomenon can be understood as follows: firstly, the deposition of Bi₂S₃ layer greatly increased the absorbance intensity of the TiO₂/CIS/BS electrodes and meanwhile enlarged optical absorption area to the near infrared spectrum, which led to an increased photocurrent density. Secondly, the TiO₂/CIS/BS electrodes may be reduced the recombination of photoexcited electrons and holes through a possible band energy cascade structure formed in CSS nanostructure (Fig. 9). In this energy gap structure, the TiO₂ nanorods and CIS and BS undergo photoexcitation simultaneously through producing electrons and holes in their own conduction and valence bands, respectively. Meanwhile, the excited electrons can transfer through conduction band from Bi₂S₃ to CuInS₂ then to TiO₂, and the excited holes pass by in the opposite direction. Due to the cascade structure, the injection ability of excited electrons is enhanced. Moreover, combining with the EIS Nyquist plots in Fig. 7, the efficient separation of photo-generated electron-hole pair and high rate of electron injection between the interfaces of heterojunction and electrolyte for the composite electrodes could enhanced the photoelectrochemical performance as well. Therefore, the cascade band structure built in TiO₂/CIS/BS electrode is advantageous to electron injection and hole recovery even though the photoelectrons in Bi₂S₃ transferring to TiO₂ through the conductor band of CIS to cause higher resistance for electrons backing to the electrolyte⁵.

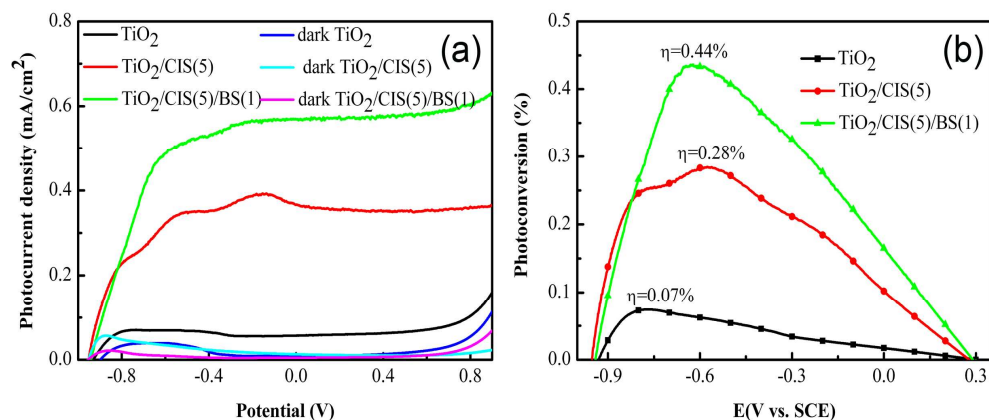


Fig. 8 Photocurrent density versus potential curves with TiO₂, TiO₂/CIS(5) CS and TiO₂/CIS(5)/BS(1) CSS electrode in dark and under the visible-light illumination of 100 mW cm⁻², respectively (a), photoconversion efficiency of TiO₂, TiO₂/CIS(5) CS and TiO₂/CIS(5)/BS(1) CSS electrodes under the visible-light illumination of 100 mW cm⁻² (b).

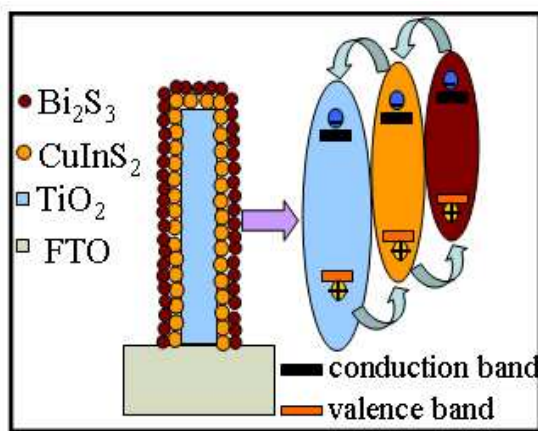


Fig. 9 The diagrammatic drawing of photo-induced charge transfer process in TiO₂/CIS/BS electrode.

4. Conclusions

In summary, the TiO₂/CuInS₂/Bi₂S₃ core/shell/shell (CSS) nanorods (NRs) structured composites electrodes were successfully built by SILAR method. The

deposition cycles of the CuInS₂ and Bi₂S₃ on TiO₂ NRs have been optimized to enhance the photoelectrochemical performance of TiO₂/CuInS₂/Bi₂S₃ CSS composites electrodes and the efficiency of composite electrode is up to 6 times high than that of plain TiO₂ NRs electrode and 1.5 times high than TiO₂/CuInS₂ CS NRs electrode. The architecture leads to a stronger light-harvesting ability and creates a higher rate of electron delivery channel when compare to the single shell TiO₂/CuInS₂ electrodes, which would promote the photo-excited electrons efficiently transfer to TiO₂ from the outer shell Bi₂S₃ through the CuInS₂ layer. In addition, the TiO₂ nanorods provide an exactly electron pathway over the large surface area. However, the efficiency of the TiO₂/CIS/BS CSS is still lower than that others, the main reason is that the band gap value difference between CIS and BS are too small. Thereafter, searching more appropriate components to improve the PEC performance of CSS nanostructure remains a further investigation in the succeeding research.

Acknowledgements

The authors acknowledge the financial supports by the National Natural Science Foundation of China (Grant No. 51471181, 51175490)

References

1. B. Liu and E. S. Aydil, *American Chemical Society*, 2009, 131, 3985-3990.
2. G. Li, Z. Liu, Z. Zhang and X. Yan, *Chinese Journal of Catalysis*, 2009, 30, 37-42.
3. B. Wang, T. Liu, C. Xia, F. Zhou, F. He, R. Liu, Y. Hu and H. Wang, *Materials Research Bulletin*, 2014, 59, 234-240.
4. X. Feng, K. Shankar, O. K. Varghese, M. Paulose, T. J. Latempa and C. A. Grimes, *Nano letters*, 2008, 8, 3781-3786.
5. P. Lv, W. Fu, H. Yang, H. Sun, Y. Chen, J. Ma, X. Zhou, L. Tian, W. Zhang, M. Li, H. Yao and D. Wu, *CrystEngComm*, 2013, 15, 7548.
6. M. Hamadianian, A. Gravand and V. Jabbari, *Materials Science in Semiconductor Processing*, 2013, 16, 1352-1359.
7. A. Colombo, C. Dragonetti, M. Magni, D. Roberto, F. Demartin, S. Caramori and C. A. Bignozzi, *ACS applied materials & interfaces*, 2014, 6, 13945-13955.
8. N. Osada, T. Oshima, S. Kuwahara, T. Toyoda, Q. Shen and K. Katayama, *Physical chemistry chemical physics : PCCP*, 2014, 16, 5774-5778.
9. F. Liu, J. Zhu, J. Wei, Y. Li, L. Hu, Y. Huang, O. Takuya, Q. Shen, T. Toyoda, B. Zhang, J. Yao and S. Dai, *The Journal of Physical Chemistry C*, 2014, 118, 214-222.
10. R. D. Schaller, V. M. Agranovich and V. I. Klimov, *Nature Physics*, 2005, 1, 189-194.
11. Y. Tak, S. J. Hong, J. S. Lee and K. Yong, *Journal of Materials Chemistry*, 2009, 19, 5945.
12. Y. Y. Wen-Tao Sun, Hua-Yong Pan, Xian-Feng Gao, Qing Chen, and Lian-Mao Peng*, *American Chemical Society*, 2008, 130, 1124-1125.
13. H. J. Lee, J.-H. Yum, H. C. Leventis, S. M. Zakeeruddin, S. A. Haque, P. Chen, S. I. Seok, M.

- Grätzel and M. K. Nazeeruddin, *The Journal of Physical Chemistry C*, 2008, 112, 11600-11608.
14. J. Gao, J. M. Luther, O. E. Semonin, R. J. Ellingson, A. J. Nozik and M. C. Beard, *Nano letters*, 2011, 11, 1002-1008.
15. M. Solís, M. E. Rincón, J. C. Calva and G. Alvarado, *Electrochimica Acta*, 2013, 112, 159-163.
16. Y. C. Lin and M. W. Lee, *Journal of the Electrochemical Society*, 2013, 161, H1-H5.
17. Z. J. Zhou, J. Q. Fan, X. Wang, W. Z. Sun, W. H. Zhou, Z. L. Du and S. X. Wu, *ACS applied materials & interfaces*, 2011, 3, 2189-2194.
18. J. Lu, Q. F. Han and Z. S. Wang, *Materials Research Bulletin*, 2012, 47, 1621-1624.
19. T. Li, X. Li, Q. Zhao and W. Teng, *Materials Research Bulletin*, 2014, 59, 227-233.
20. Y. Yan, Z. Zhou, W. Li, Y. Zhu, Y. Cheng, F. Zhao and J. Zhou, *RSC Advances*, 2014, 4, 38558.
21. W. Yue, C. Liu, Z. Qiu and M. Wang, *Solar Energy*, 2015, 113, 358-368.
22. Z. Fang, Y. Liu, Y. Fan, Y. Ni, X. Wei, K. Tang, J. Shen and Y. Chen, *The Journal of Physical Chemistry C*, 2011, 115, 13968-13976.
23. P. V. Kamat, *The Journal of Physical Chemistry C*, 2008, 112, 18737-18753.
24. S. Deka, A. Quarta, M. G. Lupo, A. Falqui, S. Boninelli, C. Giannini, G. Morello, M. De Giorgi, G. Lanzani and C. Spinella, *J. Am. Chem. Soc.*, 2009, 131, 2948-2958.
25. P. Reiss, M. Protiere and L. Li, *Small*, 2009, 5, 154-168.
26. G. Ai, R. Mo, Q. Chen, H. Xu, S. Yang, H. Li and J. Zhong, *RSC Adv.*, 2015, 5, 13544-13549.
27. X. Song, M. Wang, J. Deng, Y. Ju, T. Xing, J. Ding, Z. Yang and J. Shao, *Journal of Power Sources*, 2014, 269, 661-670.
28. K. Guo, Z. Liu, J. Han, Z. Liu, Y. Li, B. Wang, T. Cui and C. Zhou, *Physical chemistry chemical physics : PCCP*, 2014, 16, 16204-16213.

29. J. Han, Z. Liu, B. Yadian, Y. Huang, K. Guo, Z. Liu, B. Wang, Y. Li and T. Cui, *Journal of Power Sources*, 2014, 268, 388-396.
30. Y. Chen, Q. Tao, W. Fu, H. Yang, X. Zhou, Y. Zhang, S. Su, P. Wang and M. Li, *Electrochimica Acta*, 2014, 118, 176-181.
31. Y. Lu, J. Jia and G. Yi, *CrystEngComm*, 2012, 14, 3433.
32. C. C. Chang, J. K. Chen, C. P. Chen, C. H. Yang and J. Y. Chang, *ACS applied materials & interfaces*, 2013, 5, 11296-11306.
33. Y. Li, L. Wei, X. Chen, R. Zhang, X. Sui, Y. Chen, J. Jiao and L. Mei, *Nanoscale research letters*, 2013, 8, 1-7.
34. C. Chen, G. Ali, S. H. Yoo, J. M. Kum and S. O. Cho, *Journal of Materials Chemistry*, 2011, 21, 16430.
35. F. Mei, C. Liu, L. Zhang, F. Ren, L. Zhou, W. K. Zhao and Y. L. Fang, *Journal of Crystal Growth*, 2006, 292, 87-91.
36. D. Hou, X. Hu, P. Hu, W. Zhang, M. Zhang and Y. Huang, *Nanoscale*, 2013, 5, 9764-9772.
37. W.-H. Zhou, J. Jiao, Y. Zhao, X.-Y. Cheng, D.-X. Kou, Z.-J. Zhou and S.-X. Wu, *RSC Advances*, 2014, 4, 7617.
38. Z. Hao, Y. Cui and G. Wang, *Materials Letters*, 2015, 146, 77-80.
39. Y. Huang, G. Xie, S. Chen and S. Gao, *Journal of Solid State Chemistry*, 2011, 184, 502-508.
40. N. Zhang, Y. Zhang, X. Pan, X. Fu, S. Liu and Y.-J. Xu, *The Journal of Physical Chemistry C*, 2011, 115, 23501-23511.
41. H. Zhang, R. Zong, J. Zhao and Y. Zhu, *Environmental science & technology*, 2008, 42, 3803-3807.
42. Y. Hou, X.-Y. Li, Q.-D. Zhao, X. Quan and G.-H. Chen, *Advanced Functional Materials*, 2010, 20,

2165-2174.